JOURNAL OF MATERIALS SCIENCE **36** (2001) 3423–3435

A comparison of three modeling approaches for the prediction of microporosity in aluminum-silicon alloys

D. SEE, R. C. ATWOOD, P. D. LEE
Department of Materials, Imperial College, London SW7 2BP, UK
E-mail: p.d.lee@ic.ac.uk

Three computational models are presented for simulating porosity formation and growth due to hydrogen evolution in 7 wt% silicon aluminum alloy (Al7Si). The first model calculates the diffusion-limited growth of an average pore in one dimension and assumes that pore growth occurs under conditions of equiaxed grain formation. The second model uses a combined continuum-stochastic approach which determines the competitive, diffusion-limited growth of a set of stochastically-nucleated pores, assuming columnar grain growth in two dimensions. The third model applies a rule-based cellular automata technique, simulating porosity and grain growth in three dimensions. Fundamental thermodynamic and kinetic equations for each of the three models are given with their limiting assumptions. The model predictions are compared to experimental *in situ* radiographic observations of porosity growth during the solidification of Al7Si alloy. Further comparison of the models evaluates their computational speed, accuracy and relevance.

Nomenclature

Main symbols

C	concentration
D	diffusion coefficient
f	fraction solid or liquid
G	thermal gradient
H	nucleation distribution step height
$\mathbf{j}$	flux
k	partition coefficient
m	slope of liquidus on phase diagram
m_{alloy}	mass of alloy
n	number of moles
P	pressure
PD	pore density
PP	percentage porosity
$\mathbf{R}$	ideal gas constant
r	radius
R	source (of hydrogen)
S	solubility
SS	supersaturation
t	time
T	temperature
V	volume
W	weight percent
γ	surface tension
ρ	density

Superscripts and Subscripts

Al	aluminum
avg	average
e	effective property
eut	eutectic
f	final
H	hydrogen
l	liquid
L	liquidus
m	metallostatic + system
max	maximum
min	minimum
o	initial
n	nucleation
p	pore
ref	reference
s	solid
sol	solidification
Si	silicon
sys	system

1. Introduction

Metallurgists have long sought to unravel the physics of metal solidification. Their task has been particularly challenging because of the simultaneous occurrence of many interdependent events. The knowledge so far gained by the study of solidification has had tangible benefits for the casting industry; theoretical advances have enabled rapid computer simulation of both pouring and solidification phenomena in complex castings. The fluid flow and heat transfer within a solidifying metal have been correlated to the final mechanical properties; therefore, industrial casting designers may now quickly evaluate a variety of casting configurations and predict

0022–2461

the performance of a casting [1, 2]. Unfortunately, commercial simulation packages do not include diffusion, gas phase behavior and solubility kinetics; therefore, porosity formed due to these phenomena cannot be predicted. In order to allow this high level of prediction, the existing simulation packages must be significantly extended.

The two primary reasons for porosity formation within metal castings are: 1) impeded fluid flow coupled with a difference in the specific volumes of liquid and solid metal and 2) gas solubility differences between liquid and solid metal. In the first case, the liquid metal will try to flow to compensate for the liquid/solid volume change; however, the flow may be hindered by the solid which has already formed. In the literature, this type of porosity is often referred to as 'shrinkage porosity'. Pores formed by this mechanism are frequently large and irregularly-shaped.

The mechanisms behind the formation of shrinkage porosity have been described by a number of existing macroscopic flow models. Most of these models use Darcy's law in the semi-solid region to calculate a pressure drop due to restricted flow, as reviewed by Tynelius *et al*. [3] and Poirier [4]. The resultant pressure drop is then related to the percentage porosity via the ideal gas law and a surface energy term. The models have many different adjustable parameters, but only one experimentally measured response is usually used to fit them, the final percentage porosity. It should be noted, however, that these macroscopic models do not adequately describe the effect of gas evolution on pore formation. Determination of this effect requires understanding solidification and diffusion behavior on the mesoscopic and/or microscopic scales.

Solidification mechanisms control the solid morphology within the mushy zone where gas bubbles may form and grow. During directional solidification, the solid may grow as a planar interface, a cellular interface, or as columnar dendrites. Once gas pores form in the liquid metal phase, they interact with the complex structure of the developing solid. Since hydrogen is significantly less soluble in solid than in liquid aluminum, as more solid forms, the excess hydrogen from the solid is rejected into the surrounding liquid. Thus, solidification mechanisms also affect the distribution and concentration of alloy-constituent and gaseous solutes within the solidifying metal. Once released, these solutes can then diffuse throughout the casting.

In the case of a gaseous solute such as hydrogen, the dissolved gas diffuses into an area of lower concentration and existing pores may increase in size and new pores can form. The rate at which the hydrogen diffuses through the liquid depends upon the diffusion coefficient (which is a function of temperature and concentration) as well as the diffusion resistance caused by the solidification mechanisms. Therefore, accurate prediction of the formation and growth of porosity due to gas evolution requires simultaneous consideration of both solidification and diffusion events.

In this work, three models are presented which predict pore size, percentage porosity, and pore density in an aluminum alloy. The paper begins with a description of the physical system being modeled, followed by the governing equations and general physical property equations. The theory and implementation of each of the three modeling approaches is then presented. The models are compared and contrasted, first in terms of their capabilities and speeds, then by their sensitivity to key process and material parameters. Finally, the models are validated and differentiated by comparing their predictions to a series of *in situ* experimental observations of pore formation and growth in an aluminum alloy.

2. The physical system modeled: Assumptions and governing equations

The Al-Si system forms the basis of many important casting alloys and, since the prediction of porosity is most useful in alloys used primarily in the as-cast state, an aluminum-silicon (Al7Si) alloy was chosen for the model development. An idealized version of this system contains three phases (solid, liquid, and gas) and only three components (aluminum, silicon, and hydrogen). The phases consist of (1) liquid alloy with dissolved atomic hydrogen, (2) solid alloy with dissolved atomic hydrogen, and (3) gaseous molecular hydrogen. An illustration of the system modeled is shown in Fig. 1.

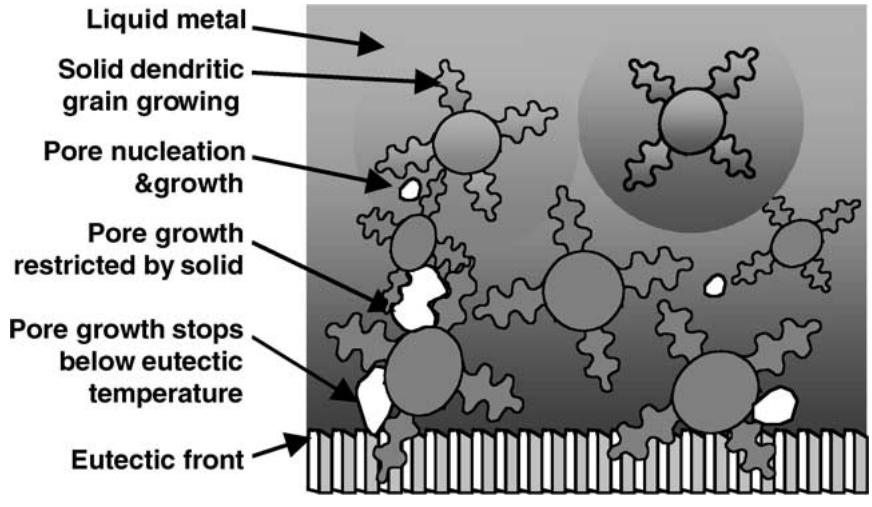

Figure 1 Schematic of the physical system being simulated.

Since diffusion of silicon is significantly slower than that of dissolved hydrogen gas, silicon diffusion was not considered in any of the three models.

Hydrogen is the only gas that has significant solubility in aluminum and the solubility of hydrogen is considerably greater in liquid aluminum than in solid aluminum [5]. As a result, when liquid aluminum containing dissolved hydrogen is cooled into the two-phase region, hydrogen is partitioned between the solid and liquid phases, with the concentration level increasing in the liquid until hydrogen gas bubbles occur. Once bubbles have formed they become sinks for supersaturated hydrogen in the liquid aluminum. Therefore, their size is dependent upon the local supersaturation in the liquid, which is a function of the hydrogen concentration and solubility. The solubility is a function of temperature, pressure and alloy composition. After solidification is complete, these bubbles become what is termed 'porosity' in the solid. Hence, to model the pore nucleation and growth, the following physics should be simulated:

1. the thermal field;
2. the flow field (for pressure and composition) and its interaction with the temperature;
3. the solutal fields for both silicon and hydrogen;
4. fraction solid (nucleation and growth of the solid grains and their interaction with the thermal and solutal fields);
5. the nucleation and growth of the gas bubbles; and
6. the impingement of the pores on the growing grains (altering both the interfacial energy and imposing curvature restrictions upon the bubbles).

The assumptions made to solve each of the above phenomena are given below, together with the governing equations derived using these assumptions. Since three different methods were used to solve these equations, the variations in the governing equations and solution techniques, together with the initial and boundary conditions used, are given afterwards in a separate section for each method.

Thermal and flow field

In this paper, the results are compared to an experimental case where the temperature field was imposed using a temperature gradient stage with a constant thermal gradient and solidification velocity, providing a constant cooling rate. All of the models were run with a constant cooling rate to match the experimental setup.

For the experimental conditions used, the mushy zone was small (less than 20 mm); therefore, the pressure change due to the volume change of the metal upon solidification was minimal [6]. Accordingly, the pressure in the liquid was assumed to be one atmosphere. The relationship between the local temperature, pressure, and volume of the pore were calculated assuming that the ideal gas law holds:

$$V_{\mathrm{p}} = \frac{n\mathbf{R}T}{P_{\mathrm{p}}} \tag{1}$$

where V_{p} is the volume occupied by the pore, n is the number of moles of H_2 in the pore, $\mathbf{R}$ is the ideal gas law constant, T is the system temperature, and P_{p} is the pressure in the pore. It is assumed that the vapor pressures of aluminum and silicon are negligible.

The pressure in the pore can be related to the pressure in the surrounding liquid metal by including the additional pressure associated with the gas-liquid interface, γ, or the Gibbs-Thompson effect. For a spherical pore:

$$P_{\mathrm{p}} = P_{\mathrm{m}} + \frac{2\gamma}{r}, \tag{2}$$

where P_{m} is the sum of the metallostatic and external pressures, γ is the gas/liquid surface energy, and r is the radius of the pore, calculated using $V_{\mathrm{p}} = 4/3\,\pi r^3$ for a sphere.

Fraction solid and solutal field for silicon

The fraction solid is a function of the nucleation and growth of the solid grains. Although the initial stage of grain nucleation and growth is treated differently in the CA model (see the separate CA model section below), all of the models assume that the evolution of fraction solid, f_{s}, is given by the Scheil equation after the dendrite tips have impinged on each other:

$$f_{\mathrm{s}} = 1 - \left(\frac{T - T_{\mathrm{Al_e}}}{m_{\mathrm{L}} W_{\mathrm{Si}}^{\mathrm{o}}}\right)^{\frac{1}{k_{\mathrm{Si}}-1}}, \tag{3}$$

where T is the temperature of the alloy, $T_{\mathrm{Al_e}}$, is the adjusted liquidus temperature of pure aluminum, m_{L} is the liquidus slope, k_{Si} is the partition coefficient for Si in aluminum and $W_{\mathrm{Si}}^{\mathrm{o}}$ is the initial weight percent of silicon. Values for $T_{\mathrm{Al_e}}$, m_{L}, k_{Si} and $W_{\mathrm{Si}}^{\mathrm{o}}$ are given in Table I. The silicon concentration in the interdendritic

TABLE I Material property constants used in the models

Constant	Symbol	Value	Source
hydrogen partition coefficient	k_{H}	0.10	estimated
silicon partition coefficient	k_{Si}	0.13	7
liquidus slope	m_{L}	−7.1212 K/wt%	calculated
system pressure	P_{m}	1.01325×10^5 Pa	set
alloy liquidus temperature	T_{L}	889.9 K	calculated
alloy eutectic temperature	T_{eut}	850.2 K	7
adjusted melting temperature of pure Al	$T_{\mathrm{Al_e}}$	939.7284 K	calculated
initial wt% of Si in the alloy	$W_{\mathrm{Si}}^{\mathrm{o}}$	7 wt%	set
surface tension	γ	856 mJ/m^2	8
liquid density	ρ_{l}	2.39 g/cm^3	7
solid density	ρ_{s}	2.55 g/cm^3	7

liquid, W_{Si}, is also given by the Scheil equation:

$$W_{Si} = W_{Si}^{o}(1 - f_s)^{k_{Si}-1}. \quad (4)$$

Solutal field for hydrogen

The nucleation and growth of the gas bubbles are directly dependent upon the local hydrogen concentration and the supersaturation. Therefore, the solutal field for hydrogen is solved directly in all three solution techniques.

The diffusion of hydrogen in the alloy is governed by [9]:

$$\frac{\partial}{\partial t}(\rho_l C_H) + \nabla \cdot \mathbf{j} = R_H, \quad (5)$$

where C_H is the concentration of dissolved atomic hydrogen in the liquid, t is time, ρ_l is the density of the liquid and R_H is the generation or consumption of hydrogen per unit volume. The concentration flux, $\mathbf{j}$, is given by:

$$\mathbf{j} = -\rho_l D_e \nabla C_H, \quad (6)$$

where D_e is the effective diffusivity given as a function of T and f_s.

Dropping the subscript H and replacing it with an s or l to denote whether C represents the hydrogen concentration in the solid or liquid, Equations 5 and 6 can be combined to obtain:

$$\frac{\partial}{\partial t}(\rho_l C_l f_l + \rho_s C_s f_s) = \nabla \cdot (\rho_l D_e \nabla C_l) + R_H. \quad (7)$$

The source term R_H represents the hydrogen increase in the liquid due to the partitioning of the dissolved hydrogen between the liquid and solid phases.

On a local or microstructural scale, it is assumed that the hydrogen concentration in the solid and liquid within a unit volume can be related by the equilibrium partition coefficient for hydrogen, i.e.:

$$C_s = k_H C_l. \quad (8)$$

Equations 7 and 8 can be combined to determine C_l:

$$\frac{\partial}{\partial t}[C_l(\rho_l f_l + k_H \rho_s f_s)] = \nabla \cdot (\rho_l D_e \nabla C_l) + R_H. \quad (9)$$

Material properties and boundary conditions

The equilibrium solubility, S_H^l, for hydrogen in aluminum/silicon alloys was derived by combining Sievert's law with a solubility expression for pure aluminum by Ransley and Neufeld [10], which was extended with the silicon correction factor given by Doutre [11]:

$$S_H^l = \sqrt{\frac{P_p}{P_{ref}}}\, 10^{\left(\frac{-2760}{T} + 2.796 - 0.0119\, W_{Si}\right)}, \quad (10)$$

where P_{ref} is the experimental reference pressure (1 atm).

The effective hydrogen diffusivity, D_e, was calculated using the solid diffusivity, D_s, and liquid diffusivity, D_l, given by Eichenauer and Markopoulos [12]:

$$D_s = 1.1 \times 10^{-1} \exp\left(-\frac{4922}{T}\right) \text{cm}^2/\text{s}, \quad [633\,\text{K} < T < 873], \quad (11)$$

$$D_l = 3.8 \times 10^{-2} \exp\left(-\frac{2315}{T}\right) \text{cm}^2/\text{s}, \quad [1053\,\text{K} < T < 1273\,\text{K}], \quad (12)$$

and the improvement on the law of mixtures suggested by Markworth [13]:

$$D_e = D_l\left(\frac{D_l(1 - f_s) + D_s(1 + f_s)}{D_l(1 + f_s) + D_s(1 - f_s)}\right). \quad (13)$$

All three models apply a zero mass flux condition at the outer boundary and assume that the gas pore/liquid alloy interface is at equilibrium. Other conditions and assumptions which differ amongst the models will be detailed in the sections below.

2.1. Deterministic (DE) model

The deterministic model is by far the simplest model, solving Equation 9 in one spatial dimension in spherical coordinates for a single, unconstrained hydrogen pore in a spherical volume of Al7Si alloy. Fig. 2 shows a schematic of the system modeled.

The DE model assumes: 1) the system being simulated is closed, spherical, and spatially isothermal; 2) the hydrogen pore is located in the center of the system and is of a known initial radius; 3) a mixture of solid and liquid alloy surrounds the pore symmetrically; 4) the liquid alloy is continuous; and 5) no hydrogen or silicon concentration gradients exist in the solid (because the solid particle size is small). In physical terms, this corresponds to a system of equally-sized pores, equally positioned throughout the alloy, and unimpeded by the solidification process.

Unlike the continuum stochastic and cellular automata models, the DE model does not include any nucleation process, but assumes nucleation has already taken place. The model simulations start with a pore of a specified size within an equilibrated system. The

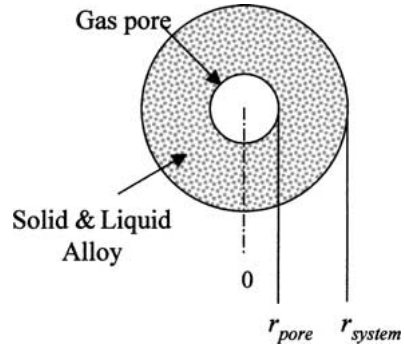

Figure 2 Schematic of the system described by the deterministic model.

starting concentration of hydrogen in the system is calculated from the initial pore radius and the equilibrium condition. The equilibrium system is perturbed by reducing temperature linearly with time; as a result, the concentration of hydrogen in the liquid/solid alloy increases, becoming supersaturated. When this occurs, a diffusion gradient forms within the liquid/solid alloy in the direction of the hydrogen pore. The pore becomes larger as the diffusing hydrogen reaches it.

The DE model differs from the continuum stochastic and the cellular automata solutions in that the modeled system is assumed to be closed, i.e. mass is conserved for both the alloy and hydrogen. Thus, the reaction term in Equation 9 is determined from a mass balance on hydrogen. Incorporating the hydrogen balance with a linear change in temperature with time, (9) becomes:

$$\frac{\partial C_l}{\partial t} = \frac{D_e}{(1 - {}^{k_H V_s}/_{V_l})} \frac{\partial C_l^2}{\partial r^2} + \frac{D_e}{(1 - {}^{k_H V_s}/_{V_l})} \frac{2}{r} \frac{\partial C_l}{\partial r} + \frac{C_l m_{alloy}}{V_l} \frac{\partial f_s}{\partial t} \left[\frac{k_H}{\rho_s} + \frac{V_s}{V_l \rho_l} \right], \quad (14)$$

where V_l and V_s are the liquid and solid volumes respectively and m_{alloy} is the total mass of alloy in the system.

The DE model was solved numerically by implementing a moving boundary, explicit finite difference technique. The initial temperature, pore size (r_{pore}), and system size (r_{sys}) were specified and the initial pore pressure, hydrogen equilibrium solubility, mass of alloy and moles of hydrogen in the system were calculated. For each subsequent time step, the system temperature was calculated using the initial temperature and a linear cooling rate. The fraction solid was calculated using the current system temperature and Equation 3. The concentration of silicon in the liquid alloy was calculated using Equation 4 and the equilibrium solubility and temperature-dependent effective diffusion coefficient were calculated using Equations 10 and 13, respectively.

Using these new values, Equation 14 was solved using central differences to determine C_l at each node between the boundaries using both Euler and fourth-order Runge-Kutta ODE integrators [14, 15]. There was no discernable difference between the computed values or in the stability using either method. Therefore, for speed, the Euler method was used with a time step of 0.001 seconds.

The concentration of hydrogen in the solid at each node was then calculated using Equation 8. The total amount of hydrogen in the liquid and solid alloy was determined by integrating over the product of the node concentration and volume. The hydrogen mole balance was then used to determine the moles of hydrogen in the pore.

2.2. Continuum stochastic (CS) model

The continuum-stochastic model simulates pore growth limited by hydrogen diffusion and the solid phase microstructure. The diffusion of hydrogen is solved on a continuum level by applying a finite difference algorithm to Equation 9. An explicit time-stepping scheme was used to capture pore nucleation with a minimal over-shoot of the nucleation supersaturation. A stochastic model of pore nucleation was implemented, as described below. Once a pore nucleates, it is coupled into the continuum model, acting as a sink or source of hydrogen. (Details of the CS model applied to aluminum-copper systems may be found in reference [16].)

The initial state of the system in the CS model was a fully molten alloy at a uniform temperature and with specified silicon and hydrogen concentrations. The initial placement of pore nuclei was randomly chosen whilst the degree of hydrogen supersaturation required to activate each nuclei was determined by assuming a statistical distribution. The model may be run with any chosen distribution of nuclei. For the cases presented here, a 'rectangular step' distribution was chosen, rising from zero to a maximum step height, H_{max} (the maximum number of potential nucleation sites), then back to zero at a later point. This distribution is characterized by a supersaturation range and a total density of nuclei; therefore, model inputs were the minimum and maximum values of the range and the total density of sites (i.e. area under the curve). Although more appropriate distributions have been suggested experimentally [17], and preliminary tests using these distributions have shown promising results, the 'rectangular step' distribution was used to keep the number of fitted parameters to a minimum.

Pore nucleation occurred when the concentration of hydrogen in a volume element exceeded the supersaturation constraint of the nucleus within the volume element. The nucleation law was based upon the assumption that a population of heterogeneous nucleation sites of various nucleation efficiencies existed within the melt, and that this nucleation efficiency resulted in a threshold supersaturation for each site. Nucleation then occurred when the supersaturation at the site exceeded the threshold:

$$\frac{C_l}{S_H^l} > SS_n, \quad (15)$$

where SS_n is the supersaturation required for nucleation. Based upon prior analysis of similar experimental results [17] a minimum threshold supersaturation, SS_{min} of 1.7 was chosen with the maximum threshold SS_{max} set to 2.2.

The solution method was as follows. At each time step T was calculated assuming a constant cooling rate and was used to determine f_s from Equation 3. The value for W_{Si} was calculated using Equation 4, and D_e and S_H^l were calculated using the material properties calculated using Equations 10 and 13. Using these updated values, Equation 9 was solved using central differences to determine C_l at each node. The potential for pores to nucleate and the growth of existing pores was then calculated. Equation 9 was only solved in two dimensions, x and y. The z dimension was set equal to the specimen thickness (2 mm) and represented by only one node.

2.3. Cellular automata model

The cellular automata (CA) model presented in this paper is a combination of a CA prediction of grain nucleation and growth (similar to that presented Rappaz and Gandin [18] and detailed elsewhere [19]) coupled to an extension of the CS model to three dimensions. The combination of the CS model with a CA model for grain growth allows the simulation of local variations which are treated as continuous averages in the DE and CS models.

The cellular automata technique assumes that the behavior of each small region or *cell* is influenced only by the conditions within that region and the conditions in neighboring regions. This technique has its origins in early simulations of nonlinear dynamics [20] and has been extensively studied from a theoretical viewpoint by number theorists and computer scientists [21, 22]. The CA model presented here is a hybrid of the discrete cellular automata described by Wolfram [22] and the continuous-valued cellular automata described by Rucker [21] in that the behavior depends upon both discrete and continuous variables. The state of each cell could either be liquid, solid, or 'growing', i.e. semi-solid; and may contain a pore. Each cell also included continuous valued variables describing the fraction solid and the concentration of the solutes. In the current implementation, only pores within a single cell were considered, and a three-dimensional grid was used.

The initial system conditions were identical to those in the CS model. The evolution of the solid phase envelopes was simulated according to the nucleation model of Rappaz *et al*. [18, 23] and a quadratic dependency of the tip growth rate on undercooling. The position of these envelopes was considered to be the position of the initial dendrite tips. The evolution of the solid phase and the concentration of silicon once the dendrite tips had passed through a cell were calculated using the Scheil equation (Equations 3 and 4).

Treatment of the diffusion of the dissolved hydrogen gas and the nucleation and growth of porosity was calculated as described in the CS section above, extended to three dimensions. The treatment of the growth of pores differed slightly - the CA model assumes that the pore lies within a single cell, even when the pore diameter exceeds the cell width, whilst the CS model allows a pore to absorb hydrogen from a larger neighborhood of cells once its diameter exceeds a control volume width.

3. Experimental methods

The growth of hydrogen pores in Al7Si alloys was observed (and quantified) *in situ* under controlled temperature conditions using an X-ray Temperature Gradient Stage (XTGS). This apparatus has been described in detail elsewhere [6], but in summary, consists of a temperature gradient stage (TGS) in combination with a micro-focus x-ray imaging system. The TGS allows the temperature gradient in the metal sample to be controlled and measured and the micro-focus x-ray system tracks pores to a resolution of 25 μm. Fig. 3 shows a schematic diagram of the XTGS experimental apparatus.

Al7Si ingots were prepared by using commercial purity aluminum and an Al12Si master alloy. The composition of the resultant Al7Si alloy was determined by using both OES analysis and ICP analysis. Table II shows the nominal composition of the Al7Si ingots. Grain refiner in the form of Ti5B rod was added to this nominal composition to obtain 0.12 ($\pm$0.008) weight percent Ti.

Prior to each run, a holding furnace was charged with approximately 6 kg of ingot and a known amount of hydrogen was dissolved in the liquid alloy by bubbling a mixture of H_2 and Ar through the melt. For each XTGS experiment, samples of Al7Si were cast directly

TABLE II Nominal composition of the Al7Si alloy

Element	Al	Si	Cu	Fe	Mn	Ti	Ni
wt.%	92.7 $\pm$1	7.05 $\pm$0.2	0.019 $\pm$0.003	0.16 $\pm$0.02	0.031 $\pm$0.004	0.010 $\pm$0.002	0.012 $\pm$0.002

All measurable elements not listed were less than 0.005 wt%.

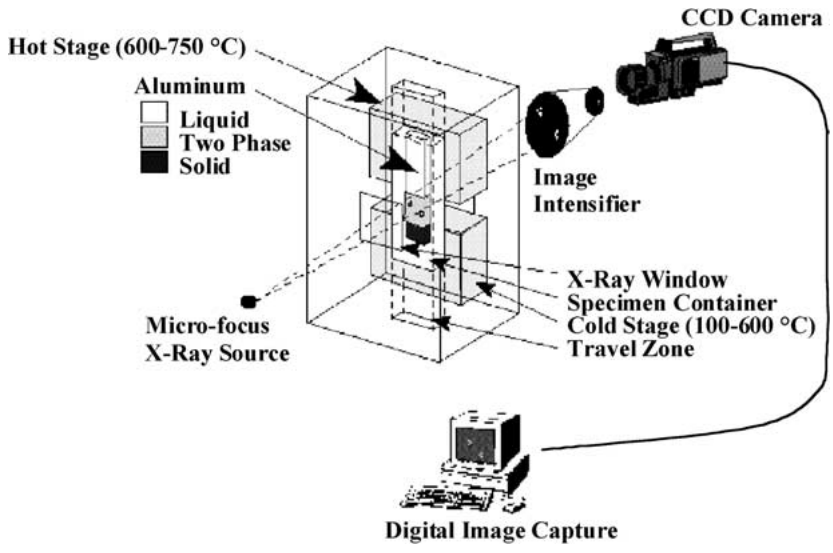

Figure 3 Schematic of the XTGS experimental setup.

TABLE III Al7Si XTGS experimental conditions

Experiment	Solidification Velocity [mm/s]	Thermal Gradient, G [°C/mm]	Solidification Time, t_{sol} [s]	Hydrogen Concentration, C_H^o [ml/100 g]
1	0.10	5.8	62	0.20
2	0.25	6.3	23	0.18
3	0.48	5.9	13	0.18

into a boron nitride specimen container placed in the hot stage of the TGS. The typical Al7Si specimen had a thickness of 2 mm, a horizontal width of 25 mm and a vertical length of 180 mm. The orientation of the XTGS was vertical with the hot stage at the top and the cold stage at the bottom. The specimen traveled from the hot stage downward to the cold stage.

Table III lists the experimental conditions for three experiments performed at different traversal velocities, providing three local solidification times, t_{sol}, in the mushy zone. Although the initial hydrogen levels was kept constant for all experiments through equilibrium with the H_2/Ar gas, Leco sub-fusion tests were also performed and are listed in Table III. These tests show minor variations between samples which are within the measurement error. Similarly a constant thermal gradient was sought, but *in situ* measurements (also listed in Table III) showed a variation from 5.8°C to 6.3°C, a minor effect in comparison to the variation in velocity.

4. Results and discussion

With the theory for each model presented, the models are compared and contrasted below, both in terms of their capabilities and speeds. This is followed by a study of their sensitivity to key process and material parameters. Finally, the models are validated against the *in situ* experimental observations of pore formation and growth.

4.1. Model comparison

The limitations and strengths of each model can be grouped into three main areas: 1) level of discretisation; 2) pore nucleation; and 3) computational speed. The first area, the level of discretisation, applies to both spatial discretisation and the extent of the region over which properties are averaged.

4.1.1. Discretisation

The models are progressively more complex in their level of spatial discretisation, with the DE, CS and CA models being respectively, 1D in spherical coordinates, 2D with finite thickness and 3D in Cartesian coordinates. For the DE and CA models, each pore acts as sphere sinking hydrogen in all directions. For the CS model, which operates in two spatial dimensions, each pore is effectively acting as a cylinder through the thickness. Hence, compared to the other models, the pores in the CS model can absorb more hydrogen from their surroundings. The CS model will therefore predict larger final pore sizes for similar input parameters to the other models. Of course the CA model can be reduced to 2D by making it only one cell thick. This was done to verify the CA model to the CS model using a grid of $100 \times 100 \times 1$ cells. The results were within 4% of each other, with this small variation attributed to not matching the exact locations and potentials of nuclei (the distributions were identical, but selection was random).

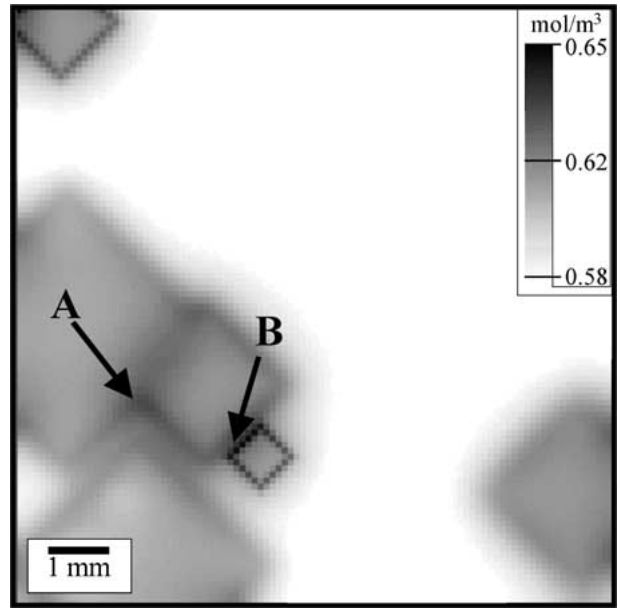

Figure 4 Illustration of the dissolved hydrogen concentration, according to the CA model, during grain envelope growth and prior to impingement. Dark areas indicate greater hydrogen buildup, and areas such as point **A** where the local geometry contains a constricted angle and point **B** where grains are near impingement and are growing into areas already enriched with hydrogen have enhanced hydrogen concentration.

The models are also progressively more complex with regards to the extent of the regions over which properties are averaged. The DE model assumes that all properties are averaged over the system with the exception of the hydrogen concentration. Hence the model is spatially isothermal and the silicon and fraction solid are also averaged. The CS model allows thermal gradients, but properties such as solid fraction and silicon concentration are determined as a function of the temperature using the Scheil equation. The CA model is the most complex; the fraction of solid may vary from cell to cell. This affects both the transport properties and the nucleation threshold values. The effect of including discrete (rather than volume-averaged) values for the fraction solid on the hydrogen concentration is illustrated by the CA results shown in Fig. 4. By resolving the growing grains, areas in which the solid restricts the diffusion path for hydrogen can be seen. The hydrogen rejected from the advancing solidification front is trapped between grains; increasing the hydrogen concentration in these regions enhances the probability of pore nucleation occurring. For example, at the point labeled **A** in Fig. 4, two grains have joined and a re-entrant angle has been produced; the hydrogen builds up in this area. At point **B**, a small grain is growing in an area in which the hydrogen has already been enriched due to

rejection from neighboring grains, hence the buildup at the advancing front of this grain is enhanced.

4.1.2. Pore nucleation

The second area where the models differ is in the treatment of pore nucleation. In the DE model, pore nucleation is not predicted. Instead, the number of activated nuclei per unit volume is implicitly set when the initial system size is set. For the sensitivity study below, and the comparison to model results later, the system size was calculated using experimentally measured pore densities. Similarly, the temperature at which the model begins calculating growth (effectively the nucleation temperature) is fixed by the assumption of an equilibrium between the hydrogen concentration within the fixed initial pore size and the surrounding aluminum. These are major limitations of the model, as it can not predict pore density and pore nucleation temperatures. However, the authors have demonstrated in an earlier publication that the nucleation temperature can be empirically derived [24]. Therefore, these restrictions could be incorporated, allowing the DE model to be implemented within a macorscopic casting simulation code and providing an extremely fast approximation of the average final pore size.

Both the CS and CA models allow the random nucleation and spacing of the pores to be simulated, overcoming the limitations of the DE model. Therefore, these models can predict the final average pore size, pore density and distribution. However, the models are not identical since the dimensionality of the simulation also influences the models' implementation of nucleation distributions. The nucleation in the CS model uses pore density per unit area for a constant thickness, whereas the CA model uses pore density per unit volume. Therefore, the CS model does not consider the effect of nearby pores in the thickness direction.

4.1.3. Computational speed

The speed of a model is dependent upon the number of degrees of freedom. The speed of the models was compared for the system size used for the sensitivity study. For the DE model, which simulates the region around a single pore, it was found that a system grid of 21 equidistant nodes was sufficient to resolve the diffusion gradient. The CS model used a grid 50×200 nodes. The CA model used a $50 \times 50 \times 5$ grid. (The results for CA baseline sensitivity study case with a $50 \times 50 \times 5$ grid were compared to a run using a $50 \times 50 \times 50$ grid identical parameters therefore the reduced grid was used for the sensitivity tests.) With these grids, the relative speed of the models was compared using the baseline sensitivity test settings (described below). The DE model ran in less than a second on a PC, whilst the CS and CA models ran on a Silicon Graphics R10K workstation in a few seconds and 15 minutes respectively. In summary, the complexity with which the discretisation and nucleation are treated is inversely proportional to the model speed, as expected.

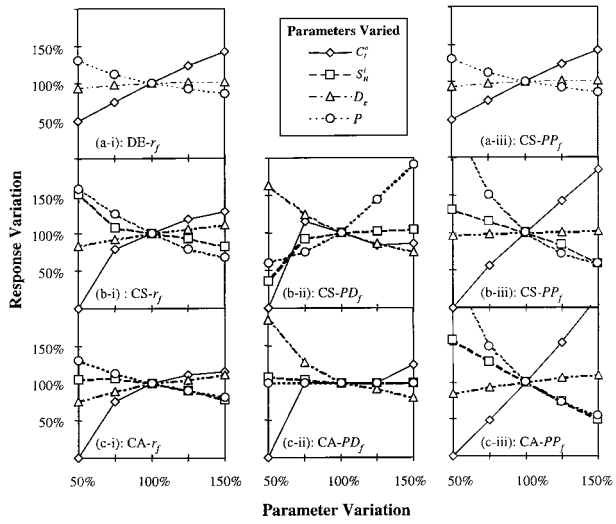

Figure 5 Sensitivity of the three responses, (i) average pore radius, r_f, (ii) pore density, PD_f, and (iii) percentage porosity, PP_f, for each of the three models, (a) DE, (b) CS and (c) CA.

4.2. Sensitivity study

The effects of varying the initial hydrogen concentration, hydrogen equilibrium solubility, effective diffusion coefficient, and system pressure were determined in each of the three models. The parameters were varied by $\pm 25\%$ and $\pm 50\%$ from their baseline values. All models used the same baseline simulation settings for comparison; these were approximately equal to those shown for experiment 2. Fig. 5 shows the results of the sensitivity tests for the DE, CS, and CA models. Finally, the sensitivity of the CS and CA models to the pore nucleation distribution is discussed.

4.2.1. Initial hydrogen concentration

Experimental work by Tynelius *et al.* [3] found that the initial hydrogen concentration had the largest influence upon the final amount of porosity in Al-Si castings. Therefore the sensitivity of each of the models to this variable was explored first. For all the models, increasing the initial hydrogen concentration increased the final pore radius (Fig. 5a-i, b-i and c-i) and percentage porosity (Fig. 5a-iii, b-iii and c-iii), correlating to Tynelius's findings. At the lowest value of initial hydrogen content, no pores were nucleated in the CS and CA models because supersaturation did not occur above the eutectic temperature.

At the highest concentration, there is a difference in the predicted final pore densities for the CS and CA models (Fig. 5b-ii and c-ii). This difference is due to local hydrogen buildup between the impinging grains of the CA model. This phenomenon is not simulated in the volume-averaged CS model.

4.2.2. Hydrogen equilibrium solubility

The equation for hydrogen solubility in the mushy zone was extrapolated from very limited data for temperatures significantly above or below those simulated. There was concern over the validity of this extrapolation, therefore the effect of varying this thermophysical

property was studied. Increasing the solubility decreases the final pore radius and percentage porosity in the CS and CA models, whilst increasing the pore number density (see Fig. 5). This is the inverse effect of hydrogen concentration, as expected.

The sensitivity of the DE model to hydrogen solubility was not simulated because it could not be tested in isolation due to the assumption of initial equilibrium hydrogen concentration.

4.2.3. Effective diffusion coefficient

For all three models, increasing the effective diffusion coefficient, D_e, increased the average pore size. By increasing the diffusion rate, more hydrogen reached the pores faster, enhancing their growth. In the case of the CS and CA models, increasing D_e decreased the total number of pores. An increased diffusivity with respect to the baseline case allowed the sink action of those pores nucleating early to lower the hydrogen concentration to a greater extent and at a greater distance, thus preventing the concentration in cells containing nucleation sites from reaching their threshold. As might be expected, decreasing D_e had the reverse effect. The pores which do nucleate then have access to larger amounts of hydrogen which is incorporated faster. The combination of these effects causes the overall percentage porosity to increase despite the decrease in pore density.

4.2.4. System pressure

It was assumed that the pressure drop in the experiments was negligible; however, this is usually not the case in an industrial casting. Therefore, the models' response to the incorporation of shrinkage (and applied pressure) was determined by testing the sensitivity to local system pressure. All the models demonstrated the expected trend, decreasing pressure increases the average final pore radius and percentage porosity. Therefore, incorporating shrinkage into the models would increase the size and amount of porosity formed.

4.2.5. Effect of nucleation distribution

The final variable tested in the sensitivity study was the effect of the nucleation distribution. The CA and CS models both require a distribution function to be input to describe the probability of pore nucleation as a function of hydrogen supersaturation. As stated in the model theory section, both the sensitivity study results above, and the comparison to experimental results below, were performed with a 'rectangular step' distribution with activation thresholds distributed from 1.7 to 2.2 times the equilibrium saturation. To test the sensitivity of the CS and CA models to the nucleation distribution, three different rectangular step distributions were tested: R1 - baseline case ($SS_{min} = 1.27, SS_{max} = 3.27, H_{max} = 2.0$), R2 - shifted to a higher supersaturation ($SS_{min} = 1.5$, $SS_{max} = 3.5$, $H_{max} = 2.0$), R3 – a narrower, but higher, step height ($SS_{min} = 1.27$, $SS_{max} = 2.27$, $H_{max} = 4.0$).

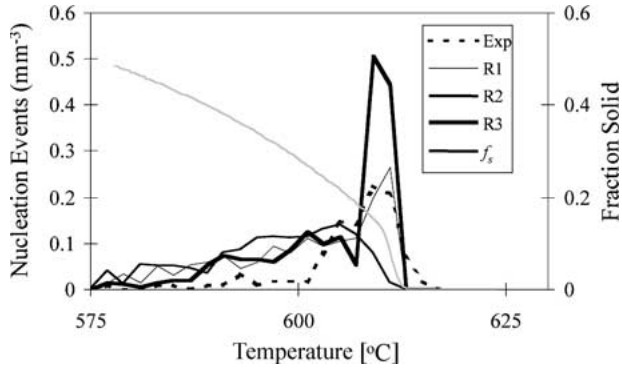

Figure 6 The number of nucleation events as a function of temperature in the CA model for three different nucleation input distributions: R1—baseline case, R2—shifted to a higher supersaturation, and R3—a narrower, but higher, step height. The fraction solid versus temperature curve is superimposed for comparison (right axis).

All initial conditions except for the nucleation function were the same as the other sensitivity studies.

The predicted histogram of nucleation events as a function of temperature is plotted in Fig. 6 for the three cases, together with the plot of fraction solid vs temperature. Although the input distribution is rectangular, the model acts as a transfer function with the number of activated nuclei being very different than the input distribution of potential nuclei. The number of pores formed in each case is equal to the area under the curve in Fig. 6. It is clearly seen that using a higher step increases the number of pores (PD_f increases by 22% for case R3 over the baseline case, R1). Interestingly, the average pore radius only differs by a few percent between these two cases—the increased numbers of pores more effectively sink the available hydrogen, producing a larger number, but only slightly smaller pores.

When the minimum threshold is increased to 1.50 (R2), the spike in the nucleation-temperature histogram just below the liquidus temperature disappears. In the baseline case, the buildup of hydrogen (due to the advancement and impingement of the modeled dendrite tip areas) results in local hydrogen concentrations which exceed the lower threshold and the sharp, stepped input nucleation distribution results in a large 'wave' of nucleation near to T_L. The CS model can not simulate this transient behavior since it simply assumes the Scheil equation. Increasing the minimum threshold eliminates the high nucleation levels at the higher temperatures; however, the amount of nucleation at lower temperatures is increased since the sinking of hydrogen is less effective. The final average pore radius for case R2 is only a few percent smaller than the baseline case, although the number of pores has decreased, and hence the percentage porosity predicted is reduced by 14%.

In summary, for all three models the predicted final pore radius and percentage porosity was found to be most sensitive to the initial hydrogen content and the local pressure, the two casting parameters that are considered experimentally to be amongst the most important. These models were less sensitive to the material property parameters and the nucleation distribution used.

TABLE IV Experimental results

Experiment	r_f	PP_f	PD_f	T_{avg}	T_{max}
	μm	%	mm^{-3}	°C	°C
1	234	1.8	0.34	608	614
2	181	2.6	0.91	608	616
3	137	1.2	1.37	593	603

4.3. Comparison to experimental results

Table IV lists the experimental results for the final average pore radius, r_f; final percent porosity, PP_f; final pore density, PD_f; average temperature of pore nucleation, T_{avg}; and maximum temperature of pore nucleation, T_{max}. The simulation results for each of the three models are listed in Table V. The correlation between experiment and the three models is shown graphically for the final pore radius and pore density in Fig. 7a and b. In this figure, the experimental and model values are plotted on the two axes against each other, clearly illustrating that all three models correctly predict the trends in the experimental data, although the three models bracket the actual data, rather than providing an exact match. The trends in the experiments that the models are illustrating are: 1) with increasing solidification velocity (increasing cooling rate) the average pore size decreases, and 2) with increasing solidification velocity (increasing cooling rate) the pore density increases. Details of the predictions for each model are discussed below.

4.3.1. DE model

The DE model simulations for each of the three experimental conditions was made by calculating the initial system volume and average pore nucleation temperature using the experimental values for pore density and T_{avg} (see Table IV), respectively. Therefore, only the final average and pore radius and percentage porosity are listed in Table V. This table and the plots of the predicted and experimentally measured average pore radius as a function of temperature in Fig. 8 illustrate that the DE model consistently under-predicts the experimental final median pore size, with the effect becoming more pronounced as the cooling rate increases. The largest deviation from the experimental values occurs at the highest cooling rate (−24%).

By altering the initial simulation temperature for experiment 3 to a higher value similar to experiments 1 and 2, the initial hydrogen concentration is increased to a value more accurately representing the initial experimental concentration. In this instance, the DE model slightly over-predicts the average pore size. This illustrates the need for an empirical function to be used to generate both the system size and the nucleation temperature.

4.3.2. CS model

Fig. 7 illustrates that the CS model has the greatest accuracy in predicting the growth of pores in the XTGS experiments, with the experimental vs. model points

TABLE V Simulation results

	DE Model				CS Model				CA Model			
Experiment	r_f	PP_f	PD_f	T_{avg}	r_f	PP_f	PD_f	T_{avg}	r_f	PP_f	PD_f	T_{avg}
	μm	%	mm^{-3}	°C	μm	%	mm^{-3}	°C	μm	%	mm^{-3}	°C
1	205	1.24	*	**	236	2.3	0.40	609	147	6.4	0.74	604
2	146	1.19	*	**	186	2.2	0.78	608	106	2.4	1.80	601
3	77	0.26	*	**	157	2.1	1.26	608	86	1.3	3.02	600
3b	124	1.09	*	881								

*system radius was calculated using this value.
**set to experimental results value.

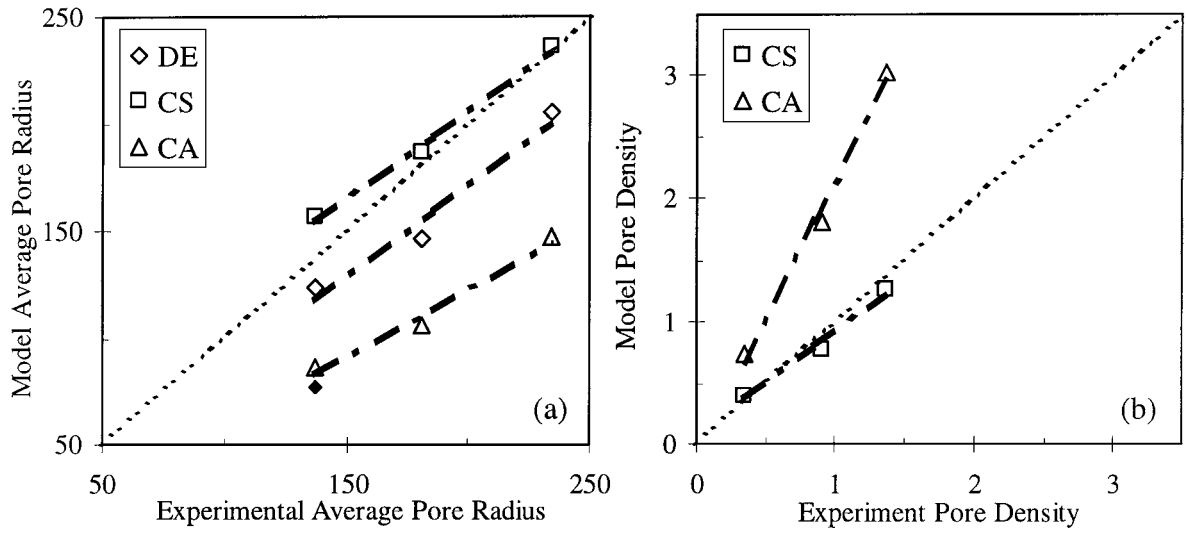

Figure 7 Correlation of each of the three model results to experiment for (a) average pore radius and (b) pore density.

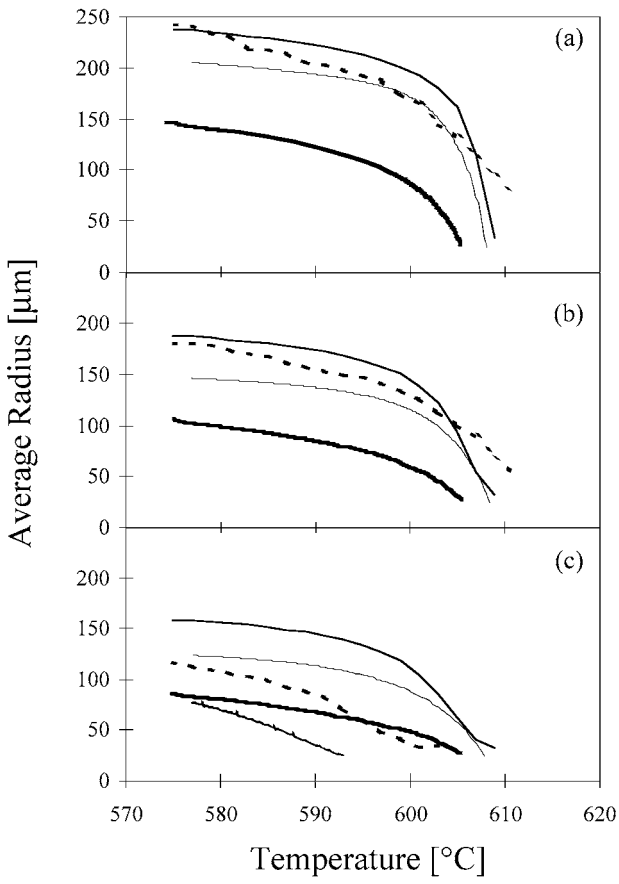

Figure 8 Comparison of experimental average pore size to the model simulations for (a) experiment 1, (b) experiment 2, and (c) experiment 3. Experimental values—dotted line, DE model—thin line (and gray line for additional case), CS model—medium thickness line, and CA model - thick line.

falling almost on the 1 : 1 line. However, this high accuracy was due to the choice of the nucleation distribution, rather than the any implicit benefits of the CS model over the other two models. The nucleation distribution was fitted to the central case with the CS model rather than the CA model because it was faster (three values of SS_{min} were tested for the medium velocity case and the value giving the most similar r_f to experiment selected). A unique feature shared by the CS and CA models is that they can simulate both the formation and growth of a *population* of gas pores. This feature is demonstrated in Fig. 9, where the experimental results are shown visually (stacked digital-video radiographs) together with the results of the CS model rendered in the same manner. In terms of understanding the development of porosity in a real casting, this capability offers distinct advantages over the DE model, which presupposes a single existing pore nucleus at the center of a representative volume. Both the CS and CA model predict the distribution of final pore sizes, together with the maximum pore size, which can be critical for properties such as fatigue [25].

Although the final descriptors of pore radius and pore density are accurately predicted by the CS model, Fig. 8 illustrates that the CS model does not accurately predict the rate of pore growth as a function of temperature. The initial rate of growth is much greater in the CS model than the experimentally observed results. The CS model's growth rate levels off whilst the experimental growth rate continues; the model finally catches up by the solidus temperature. In addition, the temperature at which the first pores nucleate varies by only a few degrees between model runs, whilst experimentally it varies by 13°C (see Table IV). As stated previously, the nucleation model was estimated, and this comparison highlights the need for improved nucleation distributions.

4.3.3. CA model

The results from the CA model are compared graphically in Fig. 8 to the XTGS experiments and visually in Fig. 9, where a unique feature of the CA model, the prediction of the grain morphology, is also illustrated. In comparison to the CS model, the CA model consistently displays smaller pores and greater pore number densities (see Fig. 7). This results from a combination of differing assumptions and solution techniques used in the models, in particular: 1) the dimensionality of the diffusion simulation, 2) differing responses to the nucleation distribution, 3) the assumed extent of the pore surface, and 4) the prediction of solid phase evolution.

The first point, the difference between the dimensionality of the diffusion simulation, was discussed earlier in the model comparison; the reduced dimensionality of the CS model causes the diffusion of hydrogen to be over-estimated, hence fewer and larger pores are predicted than in the CA model. Although the CS model more accurately predicts the final pore size (since it was used for fitting the nucleation), the CA model better predicts the rate of pore growth as a function of temperature (see Fig. 8); the problem is indeed truly three dimensional.

The second point, the differing response between the CA and CS models to the nucleation distribution, is also related to the dimensionality. The CS model overestimates the diffusion of hydrogen; therefore, the maximum supersaturation is reduced once nucleation has occurred. This in turn reduces the number of sites activated, increasing the average pore radius. Despite the use of a simplified nucleation model, the evolution of average radius with reducing temperature predicted by the CA model shows good qualitative agreement with the experimental results.

The third point, the assumed extent of the pore surface, was discussed in the model comparison; the CS model allows the pores to absorb hydrogen from a larger neighborhood of cells than the CA model, hence the reduced pore growth in the CA model.

The final point, the prediction of solid phase evolution, only has a small effect on the CA predictions because the majority of pores form after the tips of the growing dendritic grains have impinged.

In summary, all three models correctly predict the trends in the experimental data; however, their accuracy varies. The CA model incorporates the most complex physics and predicts the rate of pore growth most accurately. It also predicts the greatest number of final features: pore size, distribution, density, percentage porosity and grain morphology. The DE model is the other

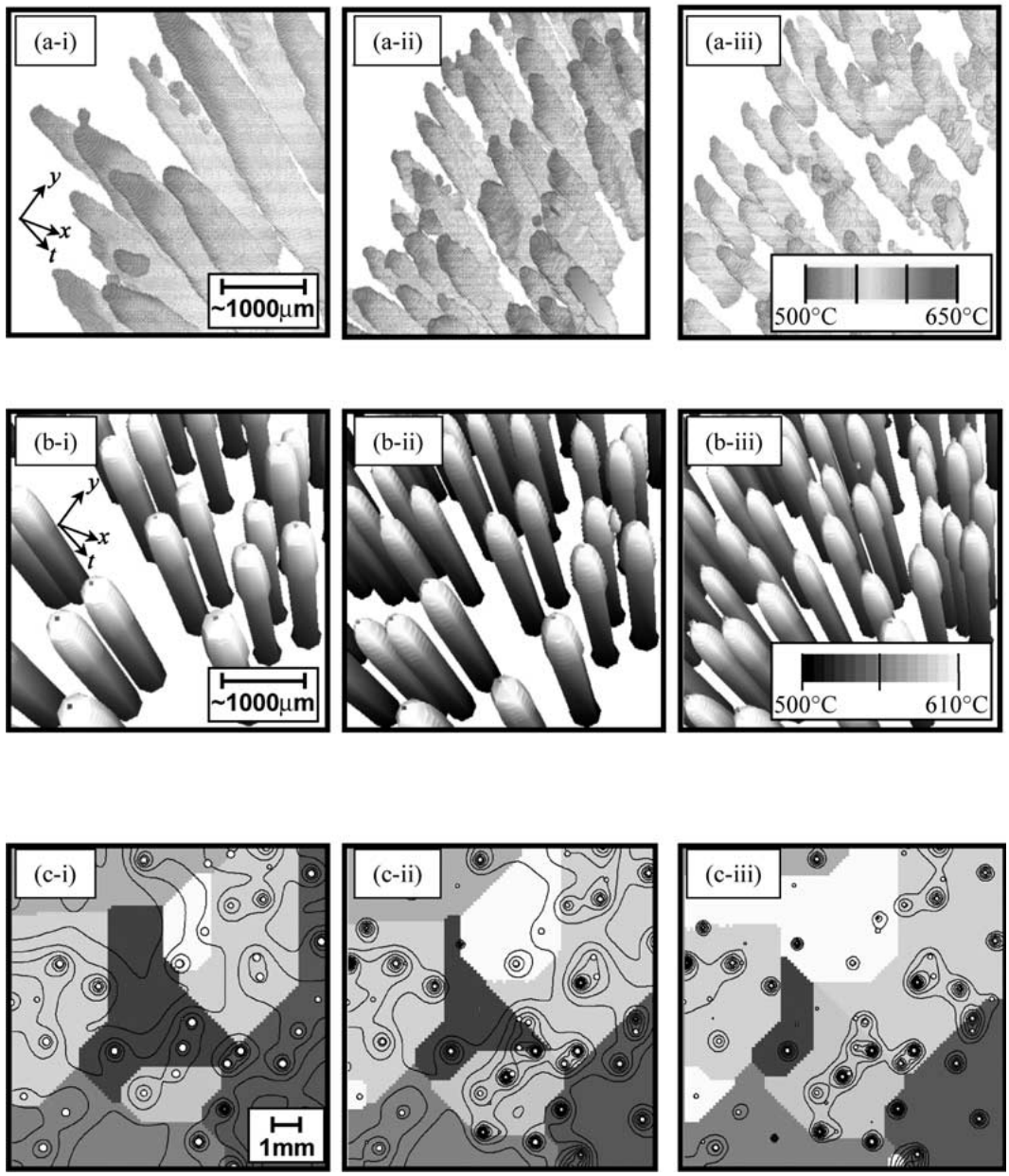

Figure 9 Comparison of output images from (a) experiment, (b) CS model, and (c) CA model (contour spacing of 0.016 mol/m^3).

extreme. It is very fast (and hence can be run as a micromodel within a macro code with minimal computational cost); however, it is dependent upon an empirically-derived system size and nucleation temperature and, consequently, it only predicts final average pore size and percentage porosity.

5. Conclusions

The DE model provides a reasonable prediction of the average final pore size when the system size and nucleation temperatures are obtained from experimental results. If this information could be obtained from other physical models, the DE model would provide a fast estimate of pore size. The DE model also serves to verify the importance of the hydrogen diffusion process in the phenomenon of porosity growth.

The CS and CA models are not dependent upon an empirically obtained system size and, even with a step nucleation model, predict the correct relationship between the final porosity and the process parameters tested. The CA model simulates a transient buildup of dissolved hydrogen during the impingement of dendrite envelopes. Although the CA model is computationally intensive, it provides an excellent tool for further exploration of the complex interaction between porosity and the developing microstructures. Although the trends were correct, these two models bracketed the actual experimental values. With an improved nucleation model for both solid phase and porosity, improved accuracy may be obtained for the case of the XTGS experiments. For application to complex industrial castings, a sensitivity study indicated that these models must be coupled to a calculation of the shrinkage pressure.

Acknowledgements

This work was funded in part by the EPSRC in collaboration with BAe, Federal-Mogul and Aeromet under grants (GR/L88351 and GR/L70042) and using computer facilities provided in part under grant GR/L86821. One of the authors (PDL) would like to thank Aisin

Takaoka for their ongoing support of his macro-micro modeling efforts. PDL would also like to thank John Hunt at the University of Oxford and Alcan International's Kingston Research and Development Center for their assistance and sponsorship of the experimental work.

References

1. J. BEECH, M. BARKHUDAROV, K. CHANG and S. B. CHIN, in Proceedings of the Eighth International Conference on Modeling of Casting and Welding Processes, San Diego, CA, June 1998, Vol. VIII, edited by B. G. Thomas and C. Beckermann (TMS, Warrendale, PA, 1998) p. 1071.
2. J. F. MAJOR, A. MAKINDE, P. D. LEE, B. CHAMBERLAIN, T. SCAPPATICCI and D. RICHMAN, *SAE Trans: J. Mater. & Man.* **103** (1994) 635.
3. K. TYNELIUS, J. F. MAJOR and D. APELIAN, *AFS Trans.* **101** (1994) 93.
4. D. R. POIRIER, in Proceedings of the Eighth International Conference on Modeling of Casting and Welding Processes, San Diego, CA, June 1998, Vol. VIII, edited by B. G. Thomas and C. Beckermann (TMS, Warrendale, PA, 1998) p. 837.
5. D. E. J. TALBOT, *Int. Metall. Rev.* **20** (1975) 166.
6. P. D. LEE and J. D. HUNT, *Acta Mater.* **45** (1993) 4155.
7. W. KURTZ and D. J. FISHER, in "Fundamentals of Solidification," 3rd ed. (Trans Tech Publications, Switzerland, 1989) p. 293.
8. J. GOICHOECHEA, C. GARCIA-CORDOVILLA, E. LOUIS and A. PARMES, *J. Mater. Sci.* **27** (1992) 5247.
9. R. B. BIRD, W. E. STEWART and E. N. LIGHTFOOT, in "Transport Phenomena" (John Wiley & Sons, New York, 1960) p. 559.
10. C. E. RANSLEY and H. NEUFELD, *J. Inst. Metals* **74** (1948) 599.
11. D. DOUTRE, Alcan International Ltd, Kingston Lab, Internal Report.
12. W. EICHENAUER and J. MARKOPOULOS, *Z. Metallkde* **65** (1974) 649.
13. A. J. MARKWORTH, *J. Mater. Sci. Lett.* **12** (1993) 1487.
14. B. A. FINLAYSON, in "Numerical Methods for Problems with Moving Fronts" (Ravenna Park Publishing, Seattle, 1992) p. 30.
15. W. H. PRESS, B. P. FLANNERY, S. A. TEUKOLSKY and W. T. VETTERLING, in "Numerical Recipes: The Art of Scientific Computing" (Cambridge University Press, 1986) p. 550.
16. P. D. LEE and J. D. HUNT, in "Modeling of Casting, Welding, and Advanced Solidification Processes VII," edited by M. Cross and J. Campbell (TMS, Warrendale, PA, 1995) p. 585.
17. R. C. ATWOOD, S. SRIDHAR and P. D. LEE, *Scripta Mater.* **41** (1999) 1255.
18. M. RAPPAZ and C. A. GANDIN, *Acta Metall.* **41** (1993) 345.
19. X. XU, R. C. ATWOOD, S. SRIDHAR, P. D. LEE, M. MCLEAN, B. DRUMMINGS, R. M. WARD and M. H. JACOBS, in Proceedings of the International Symposium on Liquid Metal Processing & Casting, Santa Fe, New Mexico, February 1999, edited A. Mitchell (AVS, 1999).
20. E. FERMI, J. PASTA and S. ULAM, "Studies of Non Linear Problems" Report LA-1940 (Los Alamos National Laboratory, 1955). Reprinted in S. ULAM, "Analogies Between Analogies" (University of California Press, Berkeley, CA, USA, 1990).
21. R. RUCKER, "Two Dimensional Continuous Valued Cellular Automata" in New Constructions in Cellular Automata (Oxford University Press, Oxford, UK) (in Press).
22. S. WOLFRAM, *Physica D* **10D** (1984) 1.
23. C. A. GANDIN and M. RAPPAZ, *Acta Mater.* **45** (1997) 2187.
24. R. C. ATWOOD, S. SRIDHAR and P. D. LEE, *Scripta Mater.* **41**(12) (1999) 1255.
25. J. F. MAJOR, *AFS Trans.* **105** (1998) 901.

Received 30 May 2000
and accepted 23 February 2001